

A wide-angle formulation of foreground filters for HI intensity mapping

Rahul Kothari^{1,2}, Roy Maartens^{2,3,4}

¹School of Physical Sciences, Indian Institute of Technology, Mandi, Himachal Pradesh, India 175001

²Department of Physics and Astronomy, University of the Western Cape, Cape Town 7535, South Africa

³Institute of Cosmology & Gravitation, University of Portsmouth, Portsmouth PO1 3FX, UK

⁴National Institute for Theoretical and Computational Sciences (NITheCS), Cape Town 7535, South Africa

E-mail: quantummechanickothari@gmail.com, roy.maartens@gmail.com

Abstract. Neutral hydrogen intensity mapping can in principle deliver rapid and large-volume cosmological surveys with exquisitely accurate redshifts that are determined directly from imaging. However, intensity maps suffer from very strong foreground contamination. Future surveys will require efficient data pipelines to remove the foregrounds and reveal the cosmological signal. It is expected that this cleaning will not remove the signal in substantial parts of the available Fourier space and that significant loss of signal due to imperfect cleaning will be confined to specific regions of Fourier space. This suggests a strategy which is useful for simplified estimates and rapid computations – i.e., to apply foreground filters that avoid the regions where loss of signal is significant. The standard Fourier-space power spectrum and foreground filters use a flat-sky approximation and thus exclude wide-angle correlations. We provide a new geometrical formulation of foreground filters in harmonic space, which naturally includes all wide-angle effects in the power spectrum. Foreground filtering leads to a loss of isotropy in Fourier space. In harmonic space this produces off-diagonal correlations. We derive analytical expressions for the generalised HI power spectrum and its cross-power with CMB lensing, for both single-dish and interferometer mode surveys. We show numerically that the off-diagonal contributions are negligible for the auto power. In the cross power, there is a non-negligible off-diagonal contribution, but only for a small interval of the largest available scales. For auto and cross power, the signal loss due to foreground avoidance decreases with increasing multipole (i.e. smaller scales), and the loss in interferometer mode is equal to, or slightly greater than, in single-dish mode. We find that the cross power in single-dish mode vanishes below a critical multipole, $\ell < \ell_0$. For an SKA-like survey, $\ell_0 \sim 20 - 40$ over redshifts $z = 1 - 3$. This feature is not seen in interferometer mode as the pertinent angular scales are larger than those allowed by the minimum baseline.

Contents

1	Introduction	1
2	Foreground filters in Fourier space	3
2.1	Survey properties	4
2.2	Filter properties	4
3	Angular power spectra	5
3.1	HI auto power	7
3.2	HI $\times\kappa$ cross power	7
4	Numerical results and discussion	8
4.1	Comparison of diagonal and off-diagonal terms	9
4.2	Power loss due to foreground filters	10
5	Conclusion and outlook	11

1 Introduction

We live in an exciting era of precision cosmology where cosmological models can be robustly tested against data from cosmic microwave background (CMB) and large-scale structure (LSS) surveys. In addition to the next-generation surveys of galaxy number counts, e.g., using the Dark Energy Spectroscopic Instrument (DESI) [1], Euclid [2], Rubin Observatory Legacy Survey of Space and Time (LSST) [3], there are intensity mapping surveys, e.g. using the Square Kilometre Array Observatory Mid-frequency telescope (SKA-Mid) [4] and the Hydrogen Intensity and Real-time Analysis eXperiment (HIRAX) [5, 6], that will target the integrated 21cm spectral line emission of neutral hydrogen (HI), the most abundant element in the Universe. HI intensity mapping (IM) surveys can cover large volumes rapidly as they do not attempt to resolve individual galaxies. In addition, extremely accurate redshifts are obtained directly from imaging, using the relation between redshift and the frequency at which the image is observed: $1 + z = \nu_{\text{em}}/\nu_{\text{obs}}$, where $\nu_{\text{em}} = 1.4$ GHz, with corresponding wavelength $\lambda_{\text{em}} \equiv \lambda_{21} = 21$ cm.

Although HI IM surveys are potentially a very promising cosmological probe, foreground contamination poses a great challenge and must be removed. The major source of contamination is Galactic synchrotron emission, due to the acceleration of cosmic ray electrons by the Galactic magnetic field, and ~ 5 orders of magnitude larger than the 21cm signal. Other sources of contamination include free-free emission (due to acceleration of electrons by ions) and extragalactic bright radio galaxies [7, 8].

Sophisticated foreground cleaning techniques have been developed for HI IM (see e.g. [9–13]). The main foregrounds are approximately spectrally smooth. Consequently, a conventional ‘blind’ foreground cleaning will always remove long-wavelength cosmological modes along the line of sight, since these modes will be indistinguishable from the foregrounds. Radial Fourier modes are $k_{\parallel} = \mu k$, where $\mu = \mathbf{n} \cdot \hat{\mathbf{k}}$ and \mathbf{n} is the line-of-sight direction. It follows that foreground cleaning will typically render the modes $|k_{\parallel}| < k_{\text{Fg}}$ unusable, for an appropriate value of the cut-off k_{Fg} . This applies to both observing modes of HI IM, i.e.,

single-dish mode (simply add the signals from all dishes) and interferometer mode (correlate all dish signals).

Interferometer-mode surveys suffer from a further problem, known as the ‘foreground wedge’ [14]. The foreground wedge arises since interferometer baselines are fixed physical lengths – which therefore probe different angular scales at different frequencies. As a consequence, intrinsically smooth-spectrum foregrounds can appear to have a more complicated spectra. This affects modes lying in a wedge $|k_{\parallel}| < (\tan \alpha) k_{\perp}$ in Fourier space, where α is described below (see Figure 1 and (2.7)). In principle, the foreground wedge contamination can be reduced by a careful inter-baseline calibration, but this has not yet been achieved [14]. In summary, a simple foreground filtering technique is to avoid contaminated long-wavelength radial modes, as well as wedge modes in the interferometer case [14–18].

As pointed out in [19], strategies to deal with foregrounds are of two kinds: (a) foreground subtraction and (b) foreground avoidance. Foreground subtraction requires modeling the foreground sources. On the other hand, foreground avoidance strategies mask the contaminated power spectrum modes. Foreground avoidance, or filtering, is based on the near-smoothness in frequency of foregrounds – which means that foregrounds occupy a compact region in Fourier space. There are limits to the accuracy of foreground models, which motivates a combination of foreground subtraction and avoidance in data pipelines. In this paper, we focus only on theoretical properties of foreground avoidance.

Foreground filtering has been described on the basis of the commonly used flat-sky (or plane-parallel) approximation in Fourier space, i.e., assuming a global, fixed line-of-sight direction \mathbf{N} . The HI brightness temperature contrast in Fourier space, $\delta_{\text{HI}}(\mathbf{k}, \mathbf{N}, z)$ leads to a Fourier power spectrum $P_{\text{HI}}(k, \mathbf{N}, z)$, which necessarily neglects wide-angle correlations. In this paper, we find a new wide-angle formulation of foreground filtering – i.e., without assuming a fixed line-of-sight – and give a geometrical interpretation. We achieve this by working with angular power spectra in harmonic space. In this approach, the HI temperature contrast is $\delta_{\text{HI}}(\mathbf{n}, z) = \sum a_{\ell m}(z) Y_{\ell m}(\mathbf{n})$, where \mathbf{n} is the line of sight to a given pixel at redshift z . This leads to an angular power spectrum that includes all angular correlations. As an application, we derive and study the foreground filtered auto-correlation HI×HI angular power spectrum.

In addition, we consider the effects of foreground filtering on the angular cross-correlation of HI and CMB lensing κ . The lensing of CMB anisotropies contains an imprint of the LSS, projected from $z = 0$ to the last scattering surface [20]. The combination of CMB lensing with galaxy number counts can improve precision and break parameter degeneracies (see [21] and references therein). The situation with HI intensity mapping is different. In contrast with galaxies, the correlation between HI intensity mapping and CMB lensing is damped by the effects of foregrounds on HI intensity. One might naively expect that unlike auto-correlations HI×HI, the cross-correlation HI× κ will not be affected by HI foregrounds, since these are uncorrelated with κ . Indeed, many previous studies neglected foreground effects (e.g. [22–27]). However, it is known that the cross-correlation of HI with photometric galaxy surveys is strongly damped – since HI IM loses long-wavelength radial information while photometric surveys lose short-wavelength radial information [9, 28, 29]. CMB lensing is a more extreme case of the loss of radial precision on small scales than photometric surveys, since there is no redshift information in the CMB lensing map. This means that the correlation HI× κ is suppressed even more than HI×photometric galaxy surveys, on account of the lack of overlap in the large-scale radial modes. Our findings are consistent with this expectation (see also [30]).

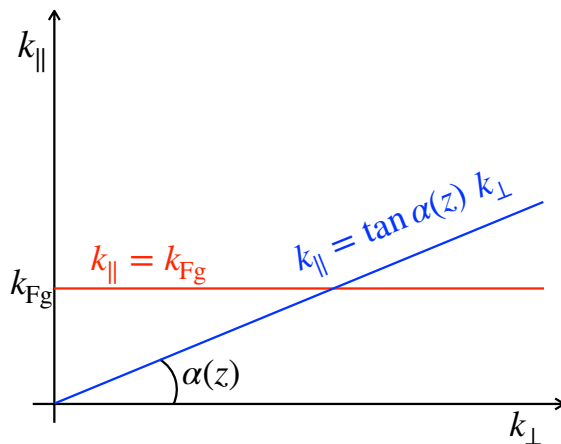


Figure 1. Schematic of foreground filter limits in Fourier space.

In order to compare theory and data, we need window functions to average HI power spectra over a redshift bin Δz , since we cannot make observations for infinitesimally thin redshift bins. Typically a top-hat window function is chosen [31]. For the auto correlations, in order to keep numerical complications under control while introducing foreground filters, we only consider a Dirac window, which corresponds to $\Delta z \rightarrow 0$ and thus gives the theoretical angular spectra. The cross correlation HI \times κ is not affected by window functions [31], since the CMB convergence field κ is redshift independent. We checked this numerically.

The remainder of the paper is structured as follows. We start by summarising foreground avoidance in Fourier space in section 2, where we also discuss the differences between the single-dish and interferometer modes of operation of HI IM surveys, including the effect of the beam in single-dish mode. A geometric interpretation of foreground filtering is developed in angular harmonic space, where all wide-angle effects are naturally included. Theoretical expressions for the generalised auto- and cross-angular power spectra with foreground filtering are derived in section 3. We present numerical results in section 4. We show that non-diagonal correlations are introduced due to foreground filtering, but that these correlations are small compared to the diagonal ones. We further show that the signal loss in cross power is in general larger than in auto power. We conclude in section 5.

We assume a fiducial Λ CDM cosmology given by *Planck* 2018 best-fit parameters [32]: $A_s = 2.101 \times 10^{-9}$, $n_s = 0.965$, $h = 0.676$, $\Omega_{b0} = 0.049$, $\Omega_{c0} = 0.261$.

2 Foreground filters in Fourier space

HI IM surveys can operate in two modes, as follows.

- Single-dish (SD) mode: auto-correlation signals from single dishes are added. This allows for probing large angular scales, but small angular scales are lost due to damping by the telescope beam.
- Interferometer (IF) mode: cross-correlated signals from the array elements are combined, allowing for high resolution on small angular scales, but with the loss of large angular modes due to a cut-off imposed by the minimum baseline.

In the absence of instrumental noise, foregrounds and other systematics, the *theoretical* HI power spectra in SD and IF modes agree on intermediate scales which are not affected by the beam (SD) or minimum baseline (IF). However the two modes have (a) different noise, (b) different effects from foregrounds, and (c) different non-foreground systematics. This means that in practice the amplitude of the observed power spectra will differ between the two survey modes, even on intermediate scales where the theoretical power spectra agree.

2.1 Survey properties

We use nominal examples of HI IM surveys in order to illustrate our results. We consider an SD-mode survey similar to that planned for SKA-Mid [4], and an IF-mode survey similar to that planned for HIRAX [5, 6]. Hereafter, we refer to these as SKA-like and HIRAX-like surveys respectively. Since we are not producing forecasts, we do not need detailed specifications for these nominal surveys. We require the redshift range, which we assume to be $1 \leq z \leq 3$ (this is realistic for SKA-Mid but extends the planned range of HIRAX). We also need the field of view for dishes with diameter D_d :

$$\theta_b = \frac{(1+z)\lambda_{21}}{D_d}, \quad \text{where } D_d = 15 \text{ m (SD), } 6 \text{ m (IF)}, \quad (2.1)$$

where the dish diameters correspond to those planned for SKA-Mid and HIRAX.

Estimates of the minimum and maximum angular scales accessible to the SKA-Mid and HIRAX-like surveys are determined in [33] (see their Fig. 6), using the validity of linear perturbations, the effect of the field of view and the sky area. Based on their results, we assume the following multipole limits for our nominal surveys:

$$\begin{aligned} \text{SD : } \ell_{\min}(z) &= 2, & \ell_{\max}(z) &= 450/(1+z), \\ \text{IF : } \ell_{\min}(z) &= 150/(1+z), & \ell_{\max}(z) &= 500. \end{aligned} \quad (2.2)$$

In the SD case, the maximum ℓ is imposed by the telescope beam. In fact, the beam damps the signal before the limit is reached, and we need to include this damping in the HI power [34]:

$$C_\ell^{\text{HI} \times \text{HI}}(z_1, z_2) \rightarrow \beta_\ell(z_1) \beta_\ell(z_2) C_\ell^{\text{HI} \times \text{HI}}(z_1, z_2), \quad (2.3)$$

$$C_\ell^{\text{HI} \times \kappa}(z) \rightarrow \beta_\ell(z) C_\ell^{\text{HI} \times \kappa}(z), \quad (2.4)$$

where the angular power spectra $C_\ell^{A \times B}$ are defined in section 3 and section 4, and the beam factor is

$$\beta_\ell(z) = \exp \left\{ -\frac{\ell(\ell+1)}{16 \ln 2} [1.22 \theta_b(z)]^2 \right\}. \quad (2.5)$$

For the IF survey the minimum in (2.2) is imposed by the minimum baseline. The maximum $\ell_{\max}^{\text{IF}} = 500$ is imposed by the range of validity of linear perturbations. We replaced the redshift-dependent value in [33] by a constant that is consistent with the limit required to safely avoid nonlinearity in the CMB lensing signal [20].

2.2 Filter properties

The radial foreground filter is applicable for both SD and IF surveys. It accounts for the loss of long-wavelength radial modes which are similar to the nearly spectrally smooth foregrounds (see Figure 1), leading to the Fourier space filter

$$|k_\parallel| > k_{\text{Fg}} = 0.01 h \text{ Mpc}^{-1} \quad (\text{SD+IF modes}), \quad (2.6)$$

where we use a value of k_{Fg} that is often chosen for next-generation surveys (e.g. [11, 15, 17, 35–37]). Here we follow the standard assumption that k_{Fg} is redshift-independent, although there is in fact a weak z -dependence [14].

The second filter applies to IF mode only. A baseline with a given physical length L probes different angular scales ℓ at various frequencies. This implies that intrinsically monochromatic emission from a foreground point source can contaminate the spectrally non-smooth signal. If it is assumed that the contamination operates within N_w primary beams of each pointing, then this leads to the exclusion of the primary beam ‘wedge’ region in (k_\perp, k_\parallel) space. The Fourier space filter is estimated as [14, 16, 17, 38, 39] (see Figure 1):

$$|k_\parallel| > \tan \alpha(z) k_\perp \quad \text{with} \quad \tan \alpha(z) = \frac{r(z)H(z) \sin [0.61 N_w \theta_b(z)]}{(1+z)} \quad (\text{IF mode}). \quad (2.7)$$

Here r is the comoving radial distance, H is the Hubble rate and θ_b is defined in (2.1). We assume that $N_w = 1$. Note that the wedge condition is not strictly a foreground-avoidance condition – in principle, the wedge can be removed with excellent calibration of baselines [14, 40], but this is currently not possible with existing technology and we treat it as futuristic.

Although the foreground filters are expressed in terms of $k_\parallel = k_z$ and $k_\perp^2 = k_x^2 + k_y^2$, they have a nice geometrical interpretation if we think in terms of k_x, k_y and k_z axes.

1. SD Mode: Only (2.6) applies, and consequently the region between the planes $k_z = \pm k_{\text{Fg}}$ is discarded.
2. IF Mode: There is ϕ symmetry and thus the wedge line (blue line in Figure 1) upon rotation about the $k_\parallel \equiv k_z$ axis generates a cone whose apex angle is $\pi/2 - \alpha$. The allowed region (2.7) is the interior of this cone – and its reflection whose axis is the negative k_z axis. Combining with the radial filter (2.6), the cones are truncated by the planes $k_z = \pm k_{\text{Fg}}$.

3 Angular power spectra

The foreground filters described above have been applied in the literature in Fourier space, for a fixed line-of-sight direction, i.e., using a flat-sky approximation. In this section, we apply the filters in angular harmonic space, which is perfectly adapted to analyse fields on the sky, including all wide-angle correlations. We therefore do not assume a fixed line of sight, i.e., we do not impose a flat-sky approximation and thus our results encompass wide-angle correlations.

For a field $X(z, \mathbf{n})$ on the sky, where \mathbf{n} is the line-of-sight direction to the field point, the spherical harmonic expansion is

$$X(z, \mathbf{n}) = \sum_{\ell \geq 0} \sum_{m=-\ell}^{\ell} a_{\ell m}^X(z) Y_{\ell m}(\mathbf{n}) \quad \text{where} \quad a_{\ell m}^X(z) = \int d\Omega_{\mathbf{n}} Y_{\ell m}^*(\mathbf{n}) X(z, \mathbf{n}). \quad (3.1)$$

Here $Y_{\ell m}(\mathbf{n})$ are spherical harmonics and $a_{\ell m}^X(z)$ are the spherical harmonic coefficients. The field X can be related to the primordial curvature perturbation $\zeta_{\mathbf{k}}$ by an angular transfer function in Fourier space, $\Delta_\ell^X(z, k)$, using the Rayleigh expansion

$$e^{i\mathbf{k}\cdot\mathbf{r}} = 4\pi \sum_{\ell, m} i^\ell j_\ell(kr) Y_{\ell m}(\mathbf{n}) Y_{\ell m}^*(\hat{\mathbf{k}}) \quad \text{where} \quad \mathbf{r} = r \mathbf{n}. \quad (3.2)$$

Here r is the line of sight distance and j_ℓ are spherical Bessel functions. Then it follows, as shown in detail in [41–44], that

$$a_{\ell m}^X(z) = 4\pi i^\ell \int_{\mathcal{D}_X} \frac{d^3\mathbf{k}}{(2\pi)^3} Y_{\ell m}^*(\hat{\mathbf{k}}) \Delta_\ell^X(k, z) \zeta_{\mathbf{k}}. \quad (3.3)$$

For example, if X is the HI brightness temperature contrast, then the dominant terms in Δ_ℓ^{HI} are given by matter density contrast and redshift space distortion terms:

$$\Delta_\ell^{\text{HI}}(k, z) = b_{\text{HI}}(z) j_\ell(kr(z)) \mathcal{T}_\delta(k, z) + \frac{(1+z)}{H(z)} k j_\ell''(kr(z)) \mathcal{T}_v(k, z). \quad (3.4)$$

Here b_{HI} is the HI bias, δ is the matter density contrast, \mathbf{v} is the peculiar velocity, and \mathcal{T} are the standard transfer functions in Fourier space:

$$\delta_{\mathbf{k}}(z) = \mathcal{T}_\delta(k, z) \zeta_{\mathbf{k}}, \quad v_{\mathbf{k}}(z) = \mathcal{T}_v(k, z) \zeta_{\mathbf{k}}. \quad (3.5)$$

In (3.3), $\mathcal{D}_X(z)$ is the region of integration in Fourier space. Thus we can study the effect of foreground filtering by restricting the region of integration for (3.3) as in Figure 1 for SD and IF modes. For later computation of angular power spectra, it is useful to write these regions in an explicit form.

1. The CMB lensing region \mathcal{D}_κ is not affected by HI foregrounds filters.
2. The HI region \mathcal{D}_{HI} follows from Figure 1. For both survey modes, $0 \leq \phi \leq 2\pi$ and $k > k_{\text{Fg}} |\sec \theta|$, where θ is restricted by

$$0 \leq \theta \leq \pi \quad (\text{SD mode}), \quad (3.6)$$

$$0 \leq \theta < \pi/2 - \alpha \quad \text{or} \quad \pi/2 + \alpha < \theta \leq \pi \quad (\text{IF mode}). \quad (3.7)$$

Since α is z dependent, so is the region of integration $\mathcal{D}_{\text{HI}}(z)$.

With this, we can now calculate the correlations amongst two fields X, Y :

$$\begin{aligned} \langle a_{\ell m}^X(z) a_{\ell' m'}^{Y*}(z') \rangle &= (4\pi)^2 i^{\ell-\ell'} \int_{\mathcal{D}_X(z)} \frac{d^3\mathbf{k}}{(2\pi)^3} \int_{\mathcal{D}_Y(z')} \frac{d^3\mathbf{k}'}{(2\pi)^3} Y_{\ell m}^*(\hat{\mathbf{k}}) Y_{\ell' m'}(\hat{\mathbf{k}}') \\ &\quad \times \Delta_\ell^X(k, z) \Delta_{\ell'}^Y(k', z') \langle \zeta_{\mathbf{k}} \zeta_{\mathbf{k}'}^* \rangle. \end{aligned} \quad (3.8)$$

We can simplify (3.8), using $\langle \zeta_{\mathbf{k}} \zeta_{\mathbf{k}'}^* \rangle = (2\pi)^3 \delta^{(3)}(\mathbf{k} - \mathbf{k}') P_\zeta(k)$, where $P_\zeta(k)$ is the primordial power spectrum:

$$\langle a_{\ell m}^X(z) a_{\ell' m'}^{Y*}(z') \rangle = \frac{2}{\pi} i^{\ell-\ell'} \int d^3\mathbf{k} Y_{\ell m}^*(\hat{\mathbf{k}}) Y_{\ell' m'}(\hat{\mathbf{k}}) \Delta_\ell^X(k, z) \Delta_{\ell'}^Y(k, z') P_\zeta(k). \quad (3.9)$$

Here the integration is performed over the region common to both $\mathcal{D}_X(z)$ and $\mathcal{D}_Y(z')$. Notice that in the absence of foreground filtering, the common region is the whole 3D space and we can perform angular integration which leads to $\delta_{\ell\ell'}$ and $\delta_{mm'}$ – as expected in the absence of foregrounds. But in the presence of foregrounds this is no longer true.

Furthermore, since $\kappa \times \kappa$ is unaffected by HI foregrounds, we only study the HI auto (HI \times HI) and cross (HI \times κ) correlations. In practice, observations of the HI brightness temperature average over finite redshift bins, which are defined by window functions. The

harmonic coefficient for any given window function $W(z, \tilde{z})$, centred at redshift z , follows from (3.3):

$$a_{\ell m}^{\text{HI}}(z) = 4\pi i^\ell \int d\tilde{z} W(z, \tilde{z}) \Delta_\ell^{\text{HI}}(k, \tilde{z}) \int_{\mathcal{D}_{\text{HI}}} \frac{d^3 \mathbf{k}}{(2\pi)^3} Y_{\ell m}^*(\hat{\mathbf{k}}) \zeta_{\mathbf{k}}. \quad (3.10)$$

However we find that significant computational complications arise with window functions when including foreground filters, and for our purposes here we show numerical results using only a Dirac window, $W(z, \tilde{z}) = \delta^{\text{D}}(z - \tilde{z})$.

3.1 HI auto power

Integration over ϕ in (3.9) gives $\delta_{mm'}$ due to axial symmetry. Then the HI correlations take the form

$$\langle a_{\ell m}^{\text{HI}}(z) a_{\ell' m'}^{\text{HI}*}(z') \rangle = f_{\ell, \ell'}^{m, m'} \delta_{mm'} \int_{Z(z, z')}^1 dx P_\ell^m(x) P_{\ell'}^{m'}(x) \mathcal{C}_{\ell \ell'}^{\text{HI, HI}}(z, z', x), \quad (3.11)$$

where we defined

$$\mathcal{C}_{\ell \ell'}^{XY}(z, z', x) = \frac{2}{\pi} \int_{k_{\text{Fg}/x}}^\infty dk k^2 \Delta_\ell^X(k, z) \Delta_{\ell'}^Y(k, z') P_\zeta(k). \quad (3.12)$$

Here $P_\ell^m(x)$ are associated Legendre polynomials, the lower limit of the x integral is

$$Z(z, z') = \begin{cases} \pi/2 & \text{for SD,} \\ \max \{ \sin \alpha(z), \sin \alpha(z') \} & \text{for IF,} \end{cases} \quad (3.13)$$

and

$$f_{\ell, \ell'}^{m, m'} = \frac{i^{\ell - \ell'}}{2} \left[1 + (-1)^{\ell + \ell' + m + m'} \right] \left[\frac{(2\ell + 1)(2\ell' + 1)(\ell - m)!(\ell' - m')!}{(\ell + m)!(\ell' + m')!} \right]^{1/2}. \quad (3.14)$$

3.2 HI $\times\kappa$ cross power

For the cross correlation, as pointed out above, \mathcal{D}_κ is the whole of Fourier space. Thus (3.9) simplifies to

$$\langle a_{\ell m}^{\text{HI}}(z) a_{\ell' m'}^{\kappa*} \rangle = f_{\ell, \ell'}^{m, m'} \delta_{mm'} \int_{\sin \alpha(z)}^1 dx P_\ell^m(x) P_{\ell'}^{m'}(x) \mathcal{C}_{\ell \ell'}^{\text{HI, } \kappa}(z, x). \quad (3.15)$$

In the case of SD mode, $\alpha = 0$.

We highlight some of the common features shared by expressions (3.11) and (3.15):

- There is an explicit m dependence and both expressions are invariant under $m \rightarrow -m$. This is a consequence of ϕ symmetry in Fourier space.
- There are off-diagonal correlations, i.e., $\Delta\ell = \ell' - \ell \neq 0$, due to the loss of θ symmetry in Fourier space (explicit in Figure 1).

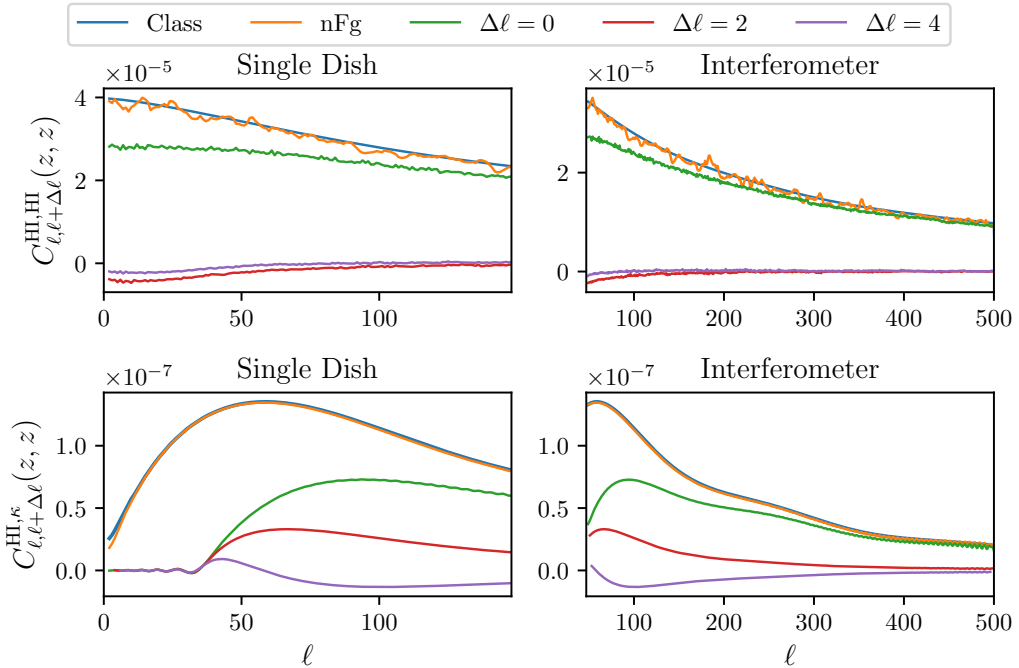


Figure 2. Effect of $\Delta\ell$ on the auto power HI \times HI (top) and cross power HI \times κ (bottom), for single-dish (left) and interferometer (right) surveys, at $z = 2$. We also make a comparison between our code (orange curves, ‘nFg’) and the `Class` code (blue curves) code in the absence of foregrounds. Our code agrees with `Class`, especially for the cross power; for auto power, numerical complications cause oscillations, even in the absence of foregrounds. Green, magenta and red curves show the effect of foreground filters for $\Delta\ell = 0, 2, 4$ respectively. (We use a Savgol filter [45] of order 4 and window size 15 for smoothing.)

- From (3.14), it is clear that $f_{\ell, \ell'}^{m, m} \neq 0$ only when $\ell + \ell'$ is even. This implies that $\Delta\ell = \ell' - \ell$ is also even, ensuring that both expressions (3.11) and (3.15) are real.

Given an m dependence and the presence of non-diagonal correlations in (3.11) and (3.15), we can define the *generalized* angular power spectra for both auto and cross correlations in the presence of foreground filters:

$$C_{\ell\ell'}^{XY}(z, z') = \sum_{m=-L}^L \frac{\langle a_{\ell m}^X(z) a_{\ell' m}^{Y*}(z') \rangle}{\sqrt{(2\ell+1)(2\ell'+1)}} \quad \text{where } L = \min\{\ell, \ell'\}. \quad (3.16)$$

In the absence of foregrounds, i.e., when $k_{\text{Fg}} \rightarrow 0$ and $\alpha \rightarrow 0$, this expression takes the expected form,

$$C_{\ell}^{XY}(z, z') = \frac{2}{\pi} \int_0^{\infty} dk k^2 \Delta_{\ell}^X(k, z) \Delta_{\ell}^Y(k, z') P_{\zeta}(k). \quad (3.17)$$

4 Numerical results and discussion

Before discussing our numerical results, we should also mention that we have benchmarked our code with `Class` as the results from both should match in the absence of foregrounds (see

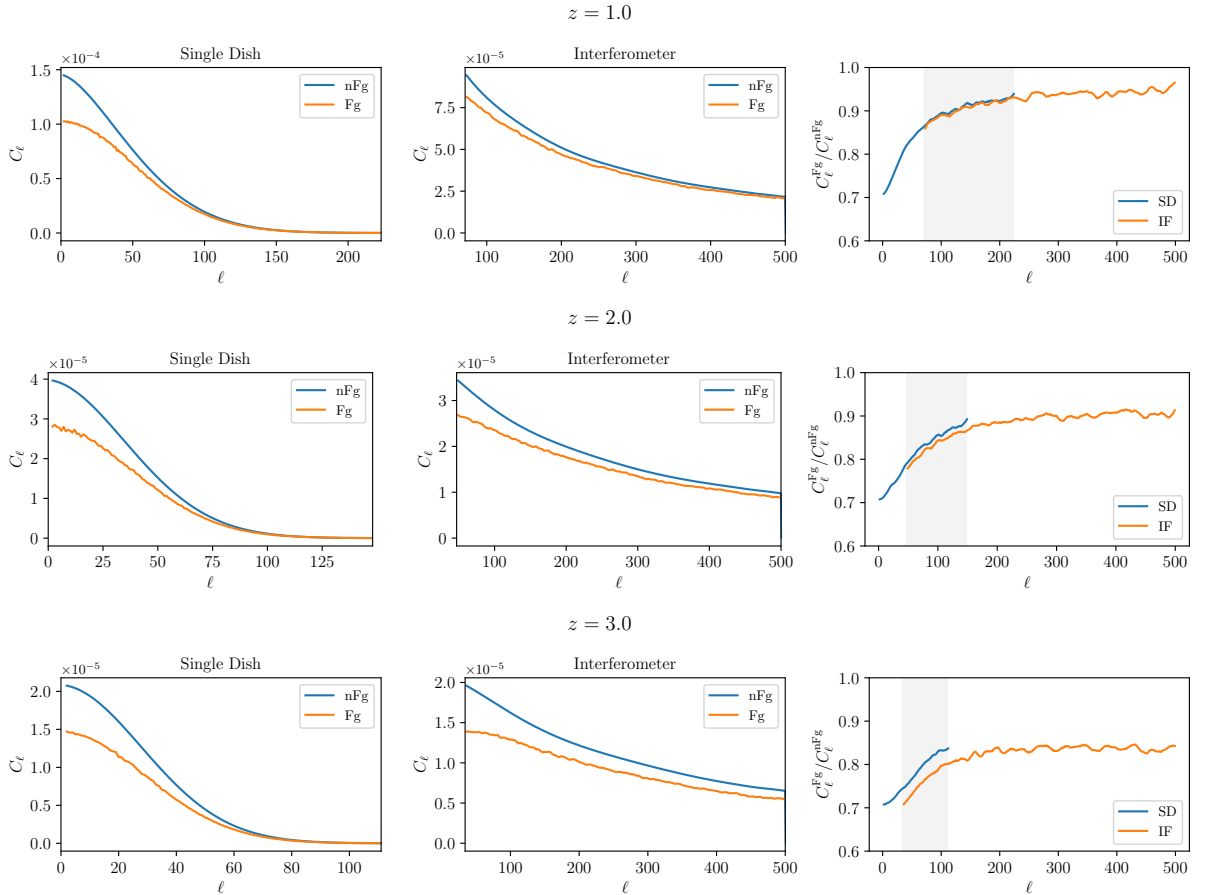


Figure 3. Foreground filtering effects on the auto HI power in SD and IF modes at $z = 1, 2, 3$. The range of ℓ values are chosen following (2.2). For each redshift, the first panel compares the SD power spectra, including the telescope beam as in (2.3). It can be seen that the beam damps the signal with increasing strength as z increases. The middle panel does the same for IF mode. The third panel compares the ratio $C_\ell^{\text{Fg}}/C_\ell^{\text{nFg}}$ for the two modes of survey. It is apparent that in the overlap range (shaded region) the power loss in SD mode is smaller than or equal to that in IF mode.

the orange and blue curves in Figure 2). For the cross power, excellent agreement is found. In case of auto power, on account of numerical complications, there are fluctuations but the match is still good.

4.1 Comparison of diagonal and off-diagonal terms

In Figure 2, we study the effect of $\Delta\ell$ on both auto and cross power spectra, as given by (3.16). The angular scales, in SD and IF modes and for auto and cross spectra, are chosen as per the discussion in §2. Beam effects are not included in this plot since our objective is only to compare relative magnitudes of power spectra for various $\Delta\ell$ values.

In the top and bottom panels, we respectively show the auto power $C_{\ell, \ell+\Delta\ell}^{\text{HI,HI}}(z, z)$ and cross power $C_{\ell, \ell+\Delta\ell}^{\text{HI,}\kappa}(z)$ at $z = 2$, for different $\Delta\ell$. The left and right panels are respectively for SD and IF modes. For the auto power HI \times HI, it is evident that the non-diagonal correlations $\ell \neq \ell'$ are negligible compared to the diagonal ones: we can safely neglect the non-diagonal correlations and take $\ell = \ell'$ in (3.16) for HI \times HI. In the cross-power case, HI \times κ , this also

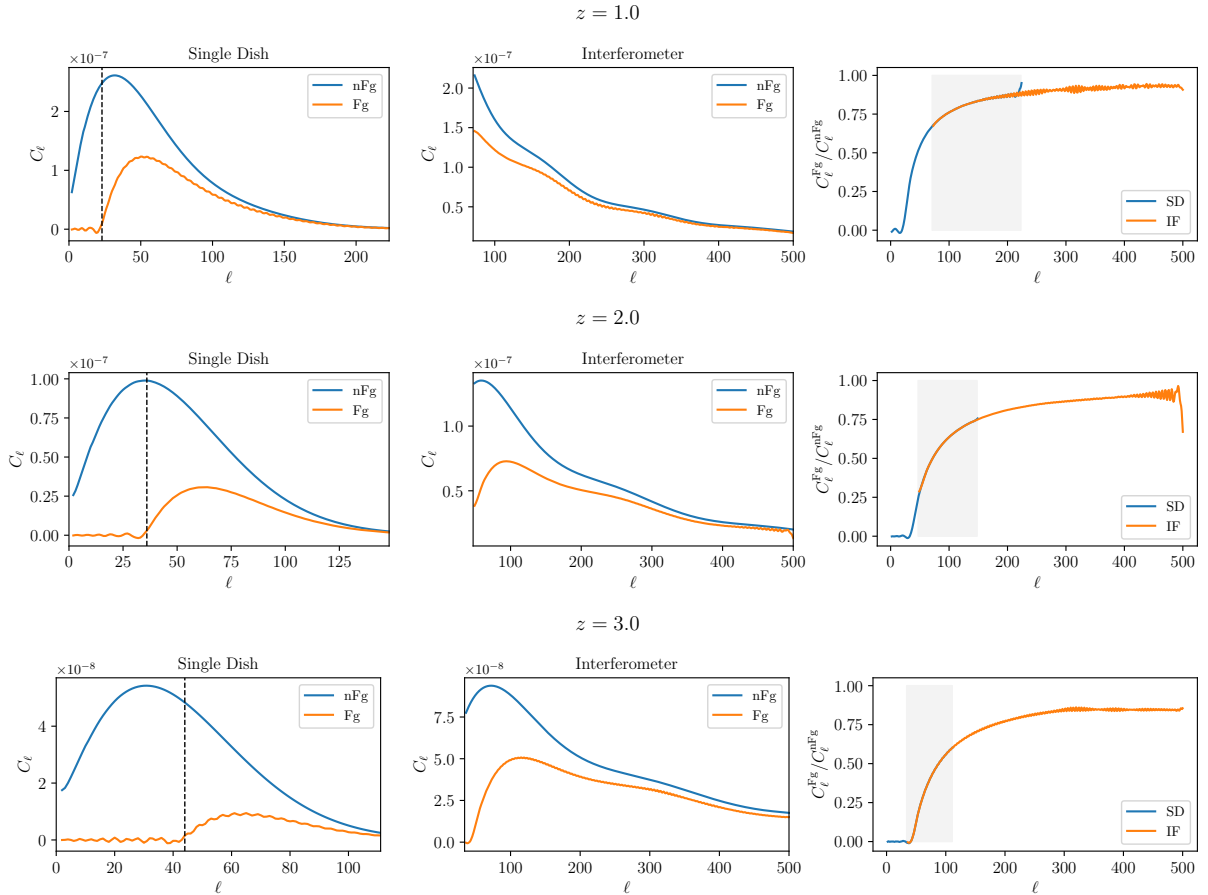


Figure 4. As in [Figure 3](#) but for the cross-power $\text{HI} \times \kappa$, including the HI telescope beam as in (2.4). In the first panels for each z , vertical dashed lines show the locations of ℓ_0 , estimated using (4.1). It is evident that the estimate of ℓ_0 is quite accurate. The third column of panels shows that the power loss is the same for both SD and IF modes in the overlap range. (On account of large oscillations at high ℓ we use a Savgol filter of larger window size 35 and order 4.)

holds for the $\Delta\ell = 4$ contributions, but the $\Delta\ell = 2$ contributions are significant for a small ℓ interval on the largest available scales. For an accurate treatment, it would be necessary to include these off-diagonal contributions, but for our purposes we will neglect them.

4.2 Power loss due to foreground filters

We further investigate both auto and cross power spectra in the presence of foregrounds, including the effect of the telescope beam in SD mode and of the minimum baseline in IF mode. Our findings are:

1. For auto spectra, [Figure 3](#) shows that the power loss in IF mode is similar to that of SD mode in the overlap region, i.e., the region of common ℓ values. Although the losses in both spectra increase as z increases, the power loss becomes more prominent for IF mode as compared to SD. This can be understood from (3.13), since increasing z leads to a larger value of $\sin\alpha$, which in turn reduces the integration range in (3.11).

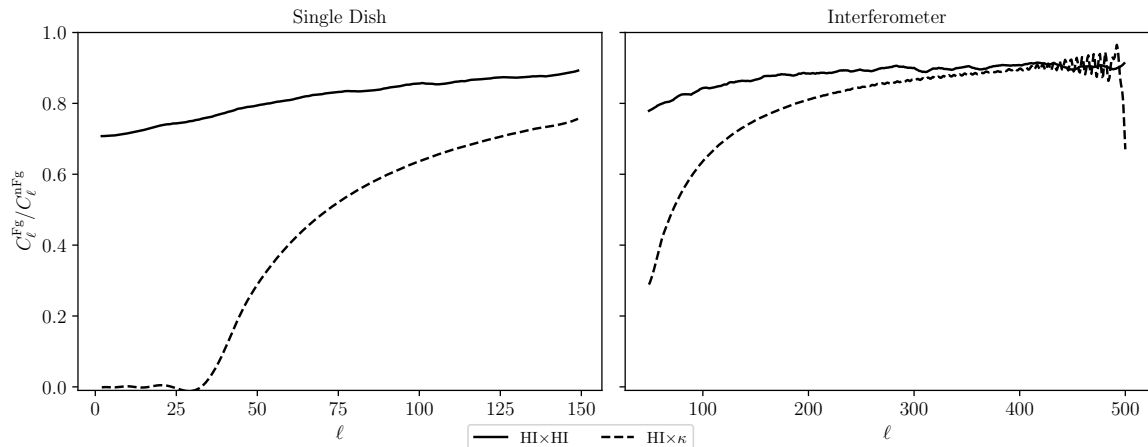


Figure 5. Comparison of $\text{HI} \times \text{HI}$ and $\text{HI} \times \kappa$ power losses due to foregrounds at $z = 2.0$. For both auto and cross power spectra, and in both modes of survey, $C_\ell^{\text{Fg}}/C_\ell^{\text{nFg}}$ increases with ℓ , so that the power loss decreases as ℓ increases. The power loss for $\text{HI} \times \kappa$ is always \geq that for $\text{HI} \times \text{HI}$.

2. In the cross-power case, $\text{HI} \times \kappa$, [Figure 4](#) shows the same trend of power reduction as a function of z . But in contrast to the auto spectra, the power reduction in the overlap region for both SD and IF modes is the same.
3. Furthermore the $\text{HI} \times \kappa$ signal vanishes for $\ell < \ell_0$. Since $\ell_0 < \ell_{\text{min}}^{\text{IF}}$, this feature is not seen in IF mode, but only in SD mode. Further, since $0 \leq x \leq 1$ [see (3.15)], we have $k > k_{\text{Fg}}/x > k_{\text{Fg}}$. Then a rough estimate of ℓ_0 is

$$\ell_0(z) \sim k_{\text{Fg}} r(z) \sim (23, 36, 44) \quad \text{for } z = (1, 2, 3). \quad (4.1)$$

These estimates match reasonably well with the values evident from [Figure 4](#) (left-most panels).

4. The $\text{HI} \times \kappa$ power is more severely affected by foregrounds than the $\text{HI} \times \text{HI}$ power in both survey modes, for all redshifts used in our analysis. In [Figure 5](#), we make a comparison of the power loss for SD and IF modes at $z = 2$. For both modes of survey, and for auto- and cross-power, the power loss decreases for larger ℓ values. When $\ell \sim 500$, the power losses in IF mode for the auto and cross spectra approach the same value.

5 Conclusion and outlook

HI intensity mapping offers a powerful new probe of cosmology. However, the exploitation of this probe requires the removal of very large foreground contamination. In this paper, we present a more modest treatment, in which filters are applied that aim to avoid the regions of serious foreground contamination. This can give an indication of what is possible, but it is clearly not a substitute for a comprehensive analysis and data pipeline that incorporate foreground cleaning.

We develop a new geometrical interpretation of foreground filtering for HI intensity mapping in harmonic space. Our analysis does not depend on a flat-sky approximation

(with its fixed line of sight) and therefore incorporates all wide-angle correlations. The main analytical results are given in (3.11)–(3.15), showing the generalised power spectra $C_{\ell,\ell'}^{\text{HI,HI}}$ and $C_{\ell,\ell'}^{\text{HI},\kappa}$.

In order to keep computational complications under control, we only present numerical results for the Dirac window choice in (3.10). The cross power $\text{HI} \times \kappa$ is independent of window functions.

As an application, we study the foreground-filtered $\text{HI} \times \text{HI}$ and $\text{HI} \times \kappa$ spectra, where κ is the CMB convergence field. We can summarise our findings as follows.

- Foreground filtering in harmonic space leads to a loss of symmetry and consequently to anisotropic angular power spectra in which there are off-diagonal correlations, $C_{\ell,\ell'} \neq 0$ for $\Delta\ell \equiv \ell' - \ell = 2, 4, \dots$. For the auto power $\text{HI} \times \text{HI}$, these off-diagonal correlations are negligible, as illustrated in Figure 2. In the cross power, $\text{HI} \times \kappa$, the $\Delta\ell = 2$ contribution is not negligible for a small interval of the largest available scales (lowest ℓ). A more accurate treatment of the cross power should include this contribution.
- When neglecting the $\ell' \neq \ell$ contributions and instrumental noise, our numerical results are well illustrated by Figure 3–Figure 5.
- The power losses due to foreground filtering for both auto- and cross-power, increase with redshift z , as expected.
- For a given z , harmonic multipole ℓ and observing mode (single-dish or interferometer), the power loss in auto-correlations $\text{HI} \times \text{HI}$ is less than or equal to that in cross-correlations $\text{HI} \times \kappa$.
- The power loss for the interferometer mode of operation is equal to, or slightly greater than, the loss for single-dish mode, on the multipole interval where both modes have signal. The approximate equality may seem surprising, since the foreground wedge avoidance affects only interferometer mode. However, this wedge loss only applies to higher multipoles, where the single-dish telescope beam has already effectively wiped out the signal. (Note also that we neglect the thermal noise, which is different for single-dish and interferometer modes.)
- The $\text{HI} \times \kappa$ power spectrum vanishes in single-dish mode for $\ell < \ell_0$, where ℓ_0 is estimated in (4.1). This feature is not seen in IF mode since $\ell_0 < \ell_{\text{min}}^{\text{IF}}$.
- The loss of power in $\text{HI} \times \kappa$, due to foreground avoidance, is less severe than in a Fourier analysis which uses the flat-sky approximation, e.g. [30] (see their Fig. 1). The flat-sky approximation neglects wide-angle correlations of HI intensity and CMB convergence at each redshift – whereas our angular cross-power spectrum includes these correlations, which reduces the loss of signal. We intend to further investigate this in a follow-up work.

Finally, our techniques are general and may be useful to derive wide-angle analytical expressions for foreground-filtered angular HI auto- and cross-bispectra (see e.g. [33, 46, 47] and references therein).

Acknowledgments

We thank Mario Ballardini, William Matthewson, Adrian Liu, Prabhakar Tiwari, Sandeep Kushwah and Richa Garg for useful comments and discussions, and the anonymous reviewer for comments that helped to improve the paper. The authors acknowledge support from the South African Radio Astronomy Observatory and National Research Foundation (Grant No. 75415). We used the HPC facilities at IIT Mandi (Grant No IITM/SG/DIS-ROS-SPA/111) and at the South African Centre for High Performance Computing (under the project *Cosmology with Radio Telescopes*, ASTRO-0945), the code `Class`, and the python packages `scipy`, `astropy` and `Camb`.

References

- [1] DESI collaboration, *The DESI Experiment Part I: Science, Targeting, and Survey Design*, [1611.00036](#).
- [2] EUCLID collaboration, *Euclid preparation: VII. Forecast validation for Euclid cosmological probes*, *Astron. Astrophys.* **642** (2020) A191 [[1910.09273](#)].
- [3] LSST DARK ENERGY SCIENCE collaboration, *The LSST Dark Energy Science Collaboration (DESC) Science Requirements Document*, [1809.01669](#).
- [4] SKA collaboration, *Cosmology with Phase 1 of the Square Kilometre Array: Red Book 2018: Technical specifications and performance forecasts*, *Publ. Astron. Soc. Austral.* **37** (2020) e007 [[1811.02743](#)].
- [5] D. Crichton et al., *Hydrogen Intensity and Real-Time Analysis Experiment: 256-element array status and overview*, *J. Astron. Telesc. Instrum. Syst.* **8** (2022) 011019 [[2109.13755](#)].
- [6] L. B. Newburgh et al., *HIRAX: A Probe of Dark Energy and Radio Transients*, *Proc. SPIE Int. Soc. Opt. Eng.* **9906** (2016) 99065X [[1607.02059](#)].
- [7] J. R. Shaw, K. Sigurdson, M. Sitwell, A. Stebbins and U.-L. Pen, *Coaxing cosmic 21 cm fluctuations from the polarized sky using m-mode analysis*, *Phys. Rev. D* **91** (2015) 083514 [[1401.2095](#)].
- [8] D. Alonso, P. Bull, P. G. Ferreira and M. G. Santos, *Blind foreground subtraction for intensity mapping experiments*, *Mon. Not. Roy. Astron. Soc.* **447** (2015) 400 [[1409.8667](#)].
- [9] S. Cunnington, L. Wolz, A. Pourtsidou and D. Bacon, *Impact of foregrounds on HI intensity mapping cross-correlations with optical surveys*, *Mon. Not. Roy. Astron. Soc.* **488** (2019) 5452 [[1904.01479](#)].
- [10] S. Cunnington, A. Pourtsidou, P. S. Soares, C. Blake and D. Bacon, *Multipole expansion for HI intensity mapping experiments: simulations and modelling*, *Mon. Not. Roy. Astron. Soc.* **496** (2020) 415 [[2002.05626](#)].
- [11] M. Spinelli, I. P. Carucci, S. Cunnington, S. E. Harper, M. O. Irfan, J. Fonseca et al., *SKAO HI intensity mapping: blind foreground subtraction challenge*, *Mon. Not. Roy. Astron. Soc.* **509** (2021) 2048 [[2107.10814](#)].
- [12] H. Wang, J. Mena-Parra, T. Chen and K. Masui, *Removing systematics-induced 21-cm foreground residuals by cross-correlating filtered data*, *Phys. Rev. D* **106** (2022) 043534 [[2203.07184](#)].
- [13] S. Cunnington et al., *The foreground transfer function for HI intensity mapping signal reconstruction: MeerKLASS and precision cosmology applications*, *Mon. Not. Roy. Astron. Soc.* **523** (2023) 2453 [[2302.07034](#)].
- [14] COSMIC VISIONS 21 CM collaboration, *Inflation and Early Dark Energy with a Stage II Hydrogen Intensity Mapping experiment*, [1810.09572](#).

- [15] P. Bull, P. G. Ferreira, P. Patel and M. G. Santos, *Late-time cosmology with 21cm intensity mapping experiments*, *Astrophys. J.* **803** (2015) 21 [[1405.1452](#)].
- [16] D. Alonso, P. G. Ferreira, M. J. Jarvis and K. Moodley, *Calibrating photometric redshifts with intensity mapping observations*, *Phys. Rev. D* **96** (2017) 043515 [[1704.01941](#)].
- [17] D. Karagiannis, A. Slosar and M. Liguori, *Forecasts on Primordial non-Gaussianity from 21 cm Intensity Mapping experiments*, *JCAP* **11** (2020) 052 [[1911.03964](#)].
- [18] P. S. Soares, S. Cunnington, A. Pourtsidou and C. Blake, *Power spectrum multipole expansion for HI intensity mapping experiments: unbiased parameter estimation*, *Mon. Not. Roy. Astron. Soc.* **502** (2021) 2549 [[2008.12102](#)].
- [19] R. Byrne, N. Mahesh, G. W. Hallinan, L. Connor, V. Ravi and T. J. W. Lazio, *21 cm Intensity Mapping with the DSA-2000*, [2311.00896](#).
- [20] A. Lewis and A. Challinor, *Weak gravitational lensing of the CMB*, *Phys. Rept.* **429** (2006) 1 [[astro-ph/0601594](#)].
- [21] S.-F. Chen, H. Lee and C. Dvorkin, *Precise and accurate cosmology with CMB \times LSS power spectra and bispectra*, *JCAP* **05** (2021) 030 [[2103.01229](#)].
- [22] T. G. Sarkar, *CMBR Weak Lensing and HI 21-cm Cross-correlation Angular Power Spectrum*, *JCAP* **02** (2010) 002 [[0908.1840](#)].
- [23] T. G. Sarkar, K. K. Datta, A. K. Pal, T. R. Choudhury and S. Bharadwaj, *The redshifted HI 21 cm signal from the post-reionization epoch: Cross-correlations with other cosmological probes*, *J. Astrophys. Astron.* **37** (2016) 26 [[1610.08181](#)].
- [24] C. B. V. Dash and T. G. Sarkar, *Constraining dark energy using the cross correlations of weak lensing with post-reionization probes of neutral hydrogen*, *JCAP* **02** (2021) 016 [[2010.05816](#)].
- [25] S. Tanaka, S. Yoshiura, K. Kubota, K. Takahashi, A. J. Nishizawa and N. Sugiyama, *Detectability of CMB Weak Lensing and HI Cross Correlation and constraints on cosmological parameters*, [1904.10363](#).
- [26] M. Ballardini, W. L. Matthewson and R. Maartens, *Constraining primordial non-Gaussianity using two galaxy surveys and CMB lensing*, *Mon. Not. Roy. Astron. Soc.* **489** (2019) 1950 [[1906.04730](#)].
- [27] M. Ballardini and R. Maartens, *Constraining the neutrino mass using a multitracer combination of two galaxy surveys and cosmic microwave background lensing*, *Mon. Not. Roy. Astron. Soc.* **510** (2022) 4295 [[2109.03763](#)].
- [28] C. Guandalin, I. P. Carucci, D. Alonso and K. Moodley, *Clustering redshifts with the 21cm-galaxy cross-bispectrum*, *Mon. Not. Roy. Astron. Soc.* **516** (2022) 3029 [[2112.05034](#)].
- [29] C. Modi, M. White, E. Castorina and A. Slosar, *Mind the gap: the power of combining photometric surveys with intensity mapping*, *JCAP* **10** (2021) 056 [[2102.08116](#)].
- [30] K. Moodley, W. Naidoo, H. Prince and A. Penin, *A cross-bispectrum estimator for CMB-HI intensity mapping correlations*, [2311.05904](#).
- [31] W. L. Matthewson and R. Durrer, *The Flat Sky Approximation to Galaxy Number Counts*, *JCAP* **02** (2021) 027 [[2006.13525](#)].
- [32] PLANCK collaboration, *Planck 2018 results. VI. Cosmological parameters*, *Astron. Astrophys.* **641** (2020) A6 [[1807.06209](#)].
- [33] R. Durrer, M. Jalilvand, R. Kothari, R. Maartens and F. Montanari, *Full-sky bispectrum in redshift space for 21cm intensity maps*, *JCAP* **12** (2020) 003 [[2008.02266](#)].
- [34] J. Fonseca, J.-A. Viljoen and R. Maartens, *Constraints on the growth rate using the observed galaxy power spectrum*, *JCAP* **12** (2019) 028 [[1907.02975](#)].

- [35] N. Sailer, E. Castorina, S. Ferraro and M. White, *Cosmology at high redshift — a probe of fundamental physics*, *JCAP* **12** (2021) 049 [[2106.09713](#)].
- [36] E. Castorina and M. White, *Measuring the growth of structure with intensity mapping surveys*, *JCAP* **06** (2019) 025 [[1902.07147](#)].
- [37] S. Cunnington, S. Camera and A. Pourtsidou, *The degeneracy between primordial non-Gaussianity and foregrounds in 21 cm intensity mapping experiments*, *Mon. Not. Roy. Astron. Soc.* **499** (2020) 4054 [[2007.12126](#)].
- [38] A. Liu, A. R. Parsons and C. M. Trott, *Epoch of reionization window. I. Mathematical formalism*, *Phys. Rev. D* **90** (2014) 023018 [[1404.2596](#)].
- [39] J. C. Pober, *The Impact of Foregrounds on Redshift Space Distortion Measurements With the Highly-Redshifted 21 cm Line*, *Mon. Not. Roy. Astron. Soc.* **447** (2015) 1705 [[1411.2050](#)].
- [40] A. Ghosh, F. Mertens and L. V. E. Koopmans, *Deconvolving the wedge: maximum-likelihood power spectra via spherical-wave visibility modelling*, *Mon. Not. Roy. Astron. Soc.* **474** (2018) 4552 [[1709.06752](#)].
- [41] C. Bonvin and R. Durrer, *What galaxy surveys really measure*, *Phys. Rev. D* **84** (2011) 063505 [[1105.5280](#)].
- [42] A. Challinor and A. Lewis, *The linear power spectrum of observed source number counts*, *Phys. Rev. D* **84** (2011) 043516 [[1105.5292](#)].
- [43] E. Di Dio, F. Montanari, J. Lesgourgues and R. Durrer, *The CLASSgal code for Relativistic Cosmological Large Scale Structure*, *JCAP* **11** (2013) 044 [[1307.1459](#)].
- [44] J. Fonseca, R. Maartens and M. G. Santos, *Synergies between intensity maps of hydrogen lines*, *Mon. Not. Roy. Astron. Soc.* **479** (2018) 3490 [[1803.07077](#)].
- [45] A. Savitzky and M. J. E. Golay, *Smoothing and differentiation of data by simplified least squares procedures.*, *Analytical Chemistry* **36** (1964) 1627.
- [46] E. Di Dio, R. Durrer, R. Maartens, F. Montanari and O. Umeh, *The Full-Sky Angular Bispectrum in Redshift Space*, *JCAP* **04** (2019) 053 [[1812.09297](#)].
- [47] R. Kothari and R. Maartens, *Lensing contribution to the 21 cm intensity bispectrum*, *Class. Quant. Grav.* **38** (2021) 095013 [[2101.11372](#)].